Article

Role of Spin Hall Effect in the Topological Side Surface Conduction

Jekwan Lee, Sangwan Sim, Soohyun Park, Chihun In, Seungwan Cho, Seungmin Lee, Soonyoung Cha, Sooun Lee, Hoil Kim, Jehyun Kim, Wooyoung Shim, Jun Sung Kim, Dohun Kim, and Hyunyong Choi

ACS Photonics, **Just Accepted Manuscript** • DOI: 10.1021/acsphotonics.8b00592 • Publication Date (Web): 22 Jul 2018

Role of Spin Hall Effect in the Topological Side Surface Conduction

Jekwan Lee,[†] *Sangwan Sim,*[§] *Soohyun Park,*[†] *Chihun In,*[†] *Seungwan Cho,*[†] *Seungmin Lee,*[†] *Soonyoung Cha,*[†] *Sooun Lee,*[∥] *Hoil Kim,*[⊥,¶] *Jehyun Kim,*[#] *Wooyoung Shim,*[∥] *Jun Sung Kim,*[⊥,¶] *Dohun Kim,*[#,*] *and Hyunyong Choi*[†,*]

[†]School of Electrical and Electronic Engineering, Yonsei University, Seoul 03722, Republic of Korea

[§]Los Alamos National Laboratory, Los Alamos, NM 87545, United States of America

[∥] Department of Material Science & Engineering, Yonsei University, Seoul 03722, Republic of Korea

[⊥]Department of Physics, Pohang University of Science and Technology (POSTECH), Pohang 37673, Republic of Korea

[¶]Center for Artificial Low Dimensional Electronic Systems, Institute for Basic Science, Pohang 37673, Republic of Korea

[#]Department of Physics and Astronomy, Institute of Applied Physics, Seoul National University, Seoul 08826, Republic of Korea

KEYWORDS: Topological insulators, plasmon, phonon, terahertz, ultrafast

ABSTRACT: The nature of spin transport in bulk and side surface of three-dimensional topological insulator thin film geometry is a relatively unexplored subject, compared to the extensively studied top and bottom surface states. Here we employ time- and space-resolved helicity-dependent photocurrent measurements to investigate the effect of optically excited bulk carriers on the spin-polarized topological side surface conduction. Time-resolved femtosecond double-pulse excitation reveals that the spin current toward the side surface arises from the bulk-originated spin Hall effect whose microscopic origin is governed by Elliott-Yafet type spin relaxation mechanism via extrinsic side jump process. Bias- and temperature-dependent measurements further confirm that the spin scattering in Bi_2Se_3 has multiple sources including impurity and electron-phonon scattering. SHE-assisted side surface spin conduction shows exceptionally large charge-to-spin conversion efficiency of 35% at 77 K, which may offer new spintronic applications of topological insulators such as spin-orbit torque or spin-flip controlled light-emitting devices.

Spin-polarized electronic transport in three-dimensional (3D) topological insulators (TIs) sets out many intriguing properties[1-7] due to characteristic spin-momentum locking of the topological surface state (TSS)[8,9]. The TSS with helical Dirac dispersion prevents elastic backscattering of electrons at an angle of π[9,10], resulting in a nanosecond-long spin-relaxation time. This heralds

many potential applications including dissipation-less spin filters, low-power consumption spintronics, and next-generation spin-orbit torque memory devices[11].

To date, in particular for the thin film geometry, studies of the charge and spin transport of TIs have focused on the top and bottom surfaces. Having Z_2 topological order, however, a full 3D nature of TIs indicates the spin-polarized electronic transport is possible through the entire surface area. This implies the topological side surfaces can also carry the spin-momentum locked electrons, although their spin polarization dynamics are largely unexplored so far. Akin to the conventional top-bulk-bottom surface coupling, an important question is the interaction kinetics of the side surfaces with the bulk states[12-16]. In particular, since most 3D TIs are unintentionally highly-doped materials with strong spin-orbit coupling, light helicity can induce spin-polarized current even in the bulk[17]. The associated study of its transport mechanism to the side surface, for example by spin Hall effect (SHE)[15] may provide an alternative view on the bulk-surface interactions in 3D TIs as well as toward practical device applications. Compared to the top and bottom surfaces, the side surface conduction also enables to study the bulk-surface spin coupling; this feature is entirely different from the conventional top and bottom surfaces dynamics, as discussed further below.

When spin-polarized electrons from the bulk states reach the side surface, further spin transport along the surface is governed by both the topological spin-momentum locking and the nature of spin-relaxation at the surface with broken inversion symmetry. Recent theories predict that a high concentration of impurities, in particular at the side surfaces, renders TIs to exhibit a long spin-relaxation time via D'yakonov-Perel (DP) mechanism[17]. Based on this fact, the accumulated spin-polarized electrons and the associated photoconductance enhancement can be observed in TI edges, which emerges from the bulk-originated SHE of electrons and the high

impurity concentration in TI surfaces[18]. Although such SHE can be identified via measuring the light-helicity-dependent local photocurrent, microscopic origins of the time-dependent dynamics and the associated spin relaxation mechanism during SHE have not been identified.

In this Letter, we present time-resolved helicity-dependent photocurrent correlation (tr-HDPC) measurements in the Bi_2Se_3 3D TI devices. The time- and space-resolved photocurrent measurements and the analysis of helicity-dependent relaxation times verify the qualitative picture suggested by Ref. 18 that HDPC indeed occurs at the side surface assisted by the bulk-originated SHE. As a key finding of the present experiment, we further show that the bias and temperature dependent spin relaxation time τ_s of the SHE-assisted transverse spin current is consistent with the spin relaxation process during the SHE-assisted spin accumulation; our lifetime analysis provides strong experimental evidences of the dominant Elliott-Yafet (EY) type mechanism. Moreover, we find that the emerged bulk SHE is governed by the side jump mechanism among other extrinsic processes such as skew scattering. For the application of harnessing the side surface as an efficient spin-polarized conducting channel, we show that the spin-polarized electrons emerged from the bulk SHE exhibit an exceptionally large charge-to-spin conversion ratio, reaching as large as 35% at 77K.

We study the 3D Bi_2Se_3 TI devices fabricated from a single crystal of Bi_2Se_3 grown using a melting method. The stoichiometric mixture of Bi and Se was heated at 850 °C for 48 hours, and then cooled to 500 °C with 2 °C/h of cooling rate. After additional 5 days of post-annealing at 500 °C, the topological surface state of the Bi_2Se_3 crystal was confirmed by the angle-resolved photoemission spectroscopy as shown in Ref. 19. A mechanically exfoliated Bi_2Se_3 flake (typical thickness of 50 nm) was transferred onto a 300 nm SiO_2/Si substrate. Contact electrodes across a

5 μm long channel were deposited by a thermal evaporator (Ti:Au = 5 nm: 120 nm) after photoresist patterning using a standard photolithography. A complete device is then annealed at 90°C for 1 hour, and stored in high vacuum (~1×10^{-5} torr) for 1 day to improve the contact characteristics. Two-terminal electronic transport measurement shows Ohmic I-V characteristics with two terminal resistance of 120 Ω, a typical value for highly doped bulk conducting Bi_2Se_3 TI devices[7].

For the tr- HDPC experiments, two ultrashort near-infrared (1.55 eV) pulses (~ 50 fs pulse width) were delivered from a 250 kHz Ti:sapphire regenerative amplifier (RegA 9050, Coherent Co.). An optical microscope with x50 objective lens (MPLFLN50x, Olympus Co.) was used to focus the two pulses (~ 2 μm spot size) onto the Bi_2Se_3 TI devices. The sample was mounted in a LN-cooled optical cryostat onto a motorized xy-translation stage (960-0070-03LS, 980-0942, EKSMA optics Co.). All measurements were performed with the plane of incidence carefully adjusted to be normal to the top surface so that our tr-HDPC measurements reflect the bulk originated photoresponse only.

Figure 1(a) shows the schematic illustration of our tr-HDPC measurements and the bulk SHE-assisted spin-polarized photocurrent along the side surface. In this geometry, normal incidence of light to the top and bottom surface guarantees that light helicity does not affect the in-plane spin polarization of the top and bottom surfaces[3]. Due to high doping, however, the bulk conduction band in TIs, in particular close to the top surface, exhibits a strongly anisotropic spin-orbit splitting as well as band bending-induced broken inversion symmetry. The circularly polarized light excites the out-of-plane spin-polarized carriers in the bulk[17]. The spin orientation of photogenerated electrons is determined by the electric field (or momentum) -dependent SHE that results in the transverse spin-polarized current. When the excited laser spot is close enough

to the side edge of lateral TI surface, the spin-polarized electrons with proper spin orientation heading to nearby side surface by SHE survive and accumulate, resulting in the increased photoconductance at the side surfaces[18] which is due to the spin momentum locking as well as because of the compatible spin orientation of the photogenerated carriers. In this manner, the side surface acts as an efficient spin-current read-out channel.

Figure 1(b) shows a typical single-pulse time-integrated photocurrent map performed using a piezo scanning mirror (GVS012, Thorlabs Co.) with unpolarized light. By positioning the longitudinal laser at y = 0 μm along the Bi_2Se_3 channel, we experimentally exclude the photothermoelectric current contribution (see the line cut of photocurrent in the Fig. 1(b), bottom panel). Figures 1(c) and 1(d) compare the helicity-dependent photocurrent data measured near the right, center, and left edge of TI surface when the transverse laser position is x = 4, 0, and -4 μm, respectively, with opposite polarity of the source-drain bias voltage V_{sd}. For measurement at x = 4 and -4 μm, the laser spot was 1 μm away from the TI channel edges. The solid curves are fits to the measured traces using the following helicity-dependent photocurrent model[3,5]:

$$I(\theta) = C\sin(2\theta) + L_1\sin(4\theta) + L_2\cos(4\theta) + D. \qquad (1)$$

Here, C is the photocurrent contribution associated with the circularly polarized light with the period of π. L_1 and L_2 are the contributions related to the linearly polarized light with the period of π/2 described by the linear photogalvanic and the photon drag effect, respectively[3,5], and D is the helicity-independent photocurrent component. Compared to the helicity dependence at x = 0 μm with dominant period of π/2, we see that the oscillatory photocurrent at both x = 4 and -4 μm are dominated by the C component associated with the spin-polarized electrons (dominant period of π), although the incident light wavevector is perpendicular to the x-y plane of the Bi_2Se_3 TI channel. Sign reversal of the C component is observed when the polarity of V_{sd} is reversed

(compare Figs. 1(c) and 1(d)) as well as when the laser excites on the opposite edge (top and bottom panel in Figs. 1(c) and 1(d)). We also note that the significant HDPC is observed only at non-zero V_{sd} even at the edges, indicating that both the bias-driven current direction and magnitude plays a crucial role in elucidating the physical origin of HDPC.

Consistent with the recent observation in Ref. 18 and the qualitative picture given above, we interpret the enhancement of C at the edges to occur in the topological side surface of the Bi_2Se_3 assisted by the bulk-generated spin polarization accumulated to the edges via SHE. Specifically, the right side panels in Figs. 1(c) and 1(d) show the schematic illustrations of the relationship between SHE and the side-surface conduction direction. In this interpretation, the spin accumulation induced by the bias-driven current density (black dashed lines) is governed by the out-of-plane spin polarization at the left and right edge of the lateral surface (blue and red arrows). We expect in principle that the spin dynamics is governed by the following two effects: (i) relatively fast spin relaxation during a bulk to side surface transport via SHE and (ii) relatively slow spin relaxation at the side surface. However, the previous study demonstrated that the spin-polarized transport time at the side surface is on the order of a few hundreds of ps due to the spin momentum locking and the DP mechanism[18]. Thus in this study, we focus on the short time scale (up to 10 ps), neglecting the effect of spin relaxation at the side surfaces, and thereby we focus on the dynamics during the bulk spin transport.

We first verify that the enhanced photocurrent at the edges indeed originates from spin-polarized carriers excited from the bulk. Normal incidence geometry ensures that the observed photocurrent is associated with the bulk-carrier generation; firstly because the carriers can be coupled to spin polarization of the top or bottom surface only when the light is injected in an oblique plane-of-incidence and secondly due to the fact that the direct excitation from the side

surface can be neglected due to the small optical cross section[18]. Figure 2(a) shows the laser power P dependent photocurrent, measured at x = 4 μm with linearly (black) and circularly (red) polarized light when V_{sd} = 0 V. The single-pulse photocurrent reverses the sign with increasing P and exhibits a super-linear behavior regardless of the incident laser polarization. This characteristic sign reversal indicates that the lifetime-limited photoconductance in the bulk and surface states saturates, and the photoconductance is dominated by the bolometric photoconductance when P > 10 μW. The bolometric photoconductance stems from the optical heating of phonon bath in heavily doped 3D TI, where the bulk states occupy a larger portion of the phonon bath than the surface; the photocurrent response in a high power regime denotes the dominant contribution of the bulk channel to the photocurrent. Using two-pulse excitation, whose inter-pulse delay is separated by a time Δt, we show in Fig. 2(b) the result of time-resolved photocurrent correlation (TRPC) measurement. The data exhibits a peak at time zero (Δt = 0), consistent with the super-linear characteristics observed in Fig. 1(a). The fast relaxation time of 1.83 ps obtained from an exponential fit strongly supports that the main contribution to the initial photocurrent relaxation is the bulk carriers[20,21].

To further examine the dynamic behavior of the bulk-induced SHE, we measured tr-HDPC at the edges. Figure 2(c) is the tr-HDPC data as a function of two-pulse delay Δt with varying probe-pulse helicity while the pump is the right-handed circularly polarized light. Distinct helicity dependence was observed. The photocurrent magnitude is maximum (minimum) when the helicity of each pulse is identical (opposite), while the decaying dynamics is fast only when the helicity of two pulses is the same. Taking the HDPC result at a fixed Δt, for example at Δt = 0, 2, 8 ps (Fig. 2(d)), we plot in Fig. 2(e) the Δt-dependent C, L_1, L_2, and D components obtained from fits to the HDPC results using Eq.(1). The components C and D show similar decaying

characteristics, which further corroborate that the topological side surface photocurrent originates from the bulk SHE-induced spin-polarized current. Clearly, L_1 and L_2 do not show such a time-dependent behavior. Therefore, we can attribute C and D components to the spin and momentum dynamics of the photogenerated bulk carriers, respectively. The measured relaxation time scale of C, together with the similar transient of D, reflects that it is the spin and momentum relaxation time of the SHE-driven spin-polarized carriers as they head toward the TI side surface.

Investigating the relationship between spin vs. momentum relaxation time (τ_s and τ_m, respectively) provides a crucial information on the spin relaxation mechanism. In metals and doped semiconductors, the spin relaxation is mostly governed by EY (DP) mechanism, which possesses a characteristic spin vs. momentum scaling as $\tau_s \propto \tau_m$ ($\tau_s \propto 1/\tau_m$)[22,23]. To correlate between τ_s and the experimentally measured time constants, we define the relaxation time constants of C and D as τ_C and τ_D, respectively, and perform a series of V_{sd} -dependent tr-HDPC measurements (see for example Fig. 3(a)). The photocurrent associated with the parameter C consists of both momentum relaxation at the bulk state extraneous to the spin and the spin relaxation of the SHE-induced spin current. Using Matthiessen's rule, this consideration can be applied to describe the relationship as

$$\tau_s = \frac{\tau_m \tau_C}{\tau_m - \tau_C}, \quad (2)$$

where we assume τ_D only reflects the momentum relaxation so that $\tau_D = \tau_m$. Figure 3(b) shows the plot of τ_s vs. τ_m with different V_{sd}. The data clearly show a positive correlation. We note that the exact proportionality is difficult to be determined in the present experiment since the proportionality between the two time constants can vary as a function of V_{sd}. Moreover, the linear relationship may not necessarily hold if multiple spin-scattering sources of EY mechanism are

present (e.g. impurities of different species, phonons, etc.). However, the positive correlation should be satisfied even in this scenario, so that the observed proportional relationship between τ_s and τ_m suggests that the spin relaxation during SHE is dominated by the EY mechanism. Below, by showing similar analysis as a function of T, we further show that multiple spin-scattering sources are indeed present in the Bi_2Se_3 TI.

Spin Hall effect in semiconductors is known to be dominated by various scattering mechanisms such as skew scattering or side jump process. While both mechanisms have an impurity scattering as a common origin, the Boltzmann transport theory suggests that the side jump process is responsible if the spin transport lifetime, represented by τ_C (V_{sd}) in our experiment, is independent of spin-Hall conductance $G_{SH} = I_{ph,C}/V_{sd}$ [15]. Figure 3(c) shows that G_{SH} is indeed independent of τ_C which suggests that the side jump process is the origin of the SHE-induced spin-polarized current. Meanwhile, V_{sd} also controls the amount of charge injection to the channel so that the relative ratio between the measured spin-dependent and the spin-independent photocurrent $I_{ph,C/D}$ can be interpreted as a charge-to-spin conversion efficiency[24-26]. The measured efficiency is exceptionally large, reaching above 35% (Fig. 3(c), inset), which is the largest value compared to 33% in a best-known tungsten thin films on CoFeB[25]. We also note that this efficiency does not degrade even at high V_{sd}, showing that the Bi_2Se_3 SHE-assisted side-surface channel can support a large magnitude of spin-polarized current. Further experimental investigations such as spin-orbit torque measurements using a ferromagnetic metal may be necessary to understand the extraordinarily large charge-to-spin conversion efficiency in the bulk TI states.

Having confirmed the leading role of EY mechanism and side jump process to the spin relaxation during SHE, we now show that the spin transport in the TI bulk contains multiple EY

scattering sources by performing *T*- and fluence-dependent tr-HDPC measurements; for example, see in Fig. 4(a) for the *T*-dependent tr-HDPC. Similar to the V_{sd}-dependent analysis, we identify the EY spin relaxation-dominated mechanism, which is followed by the observed positive and highly nonlinear correlation between τ_s vs. τ_m as shown in Fig. 4(b). Considering the fact that standard EY mechanism can be expressed by a linear relationship between τ_s and τ_m with impurity scattering regime, this feature suggests that the scattering source other than impurity also plays a significant role. In this experiment, increasing *T* can affect either hot-electron generation or lattice heating. To resolve this issue, we perform the pump-fluence *F* dependent tr-HDPC measurements with a fixed V_{sd} of 0.4 V. As shown in Fig. 4(c), τ_s does not vary significantly with *F*. Based on the observation, we rule out the hot-electron generation as the primary factor in the *T*-dependent spin transport dynamics. Rather, prior investigations in the Bi_2Se_3 thin films have shown that a strong intrinsic electron-phonon deformation potential is in the order of 20 eV, which poses a limit on the electronic mobility at finite *T* [27]; based on which, we attribute the electron-phonon scattering to the main source of the additional EY scattering. Thus, based on the observed V_{sd} and *T* dependence, we conclude that SHE in our doped Bi_2Se_3 device is governed by EY relaxation mechanism with electron-acoustic phonon and impurity scattering as the main spin-scattering sources.

In conclusion, a series of tr-HDPC measurements near the edge of the 3D TI geometry show that the spin-polarized side surface conduction stems from the bulk-generated SHE, during which EY mechanism and side jump process dominates the spin relaxation. We also show that the main spin-scattering sources of EY mechanism are the impurity and electron-phonon scatterings. Since the measured charge-to-spin conversion efficiency of 35 % is extremely large, we expect that our results are important in seeking an efficient route to further engineer the bulk-

surface spin coupling and the spin-polarized photocurrent enhancement, which may provide a second look toward new TI-based spintronic applications.

FIGURES

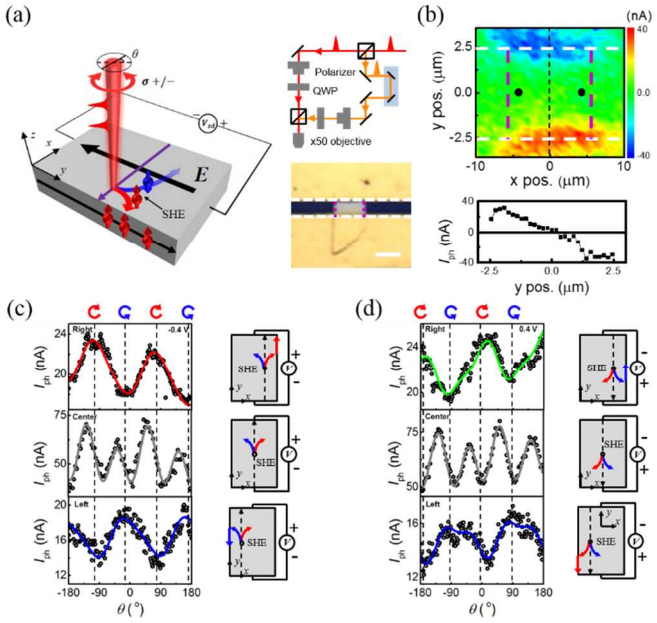

Figure 1. (a) An overview of the experiment. Main panel: Schematic illustration of the spin-polarized photocurrent signal generation. External field E from the bias voltage V_{sd} generates the spin current (purple arrow) due to the spin Hall effect (SHE). Right top panel: Schematic diagram for the time-resolved photocurrent measurements. The femtosecond laser is split and combined via a non-polarizing beam splitter. A mechanical delay stage is placed to control the two-pulse delay Δt for the time-resolved measurement. Right bottom panel: Optical image of the Bi_2Se_3 two-terminal device. The scale bar is 10 μm. (b) A typical two-dimensional (2D) photocurrent map is shown when V_{sd} = 0 V. Black dots on the contour plot indicate the transverse position at x = 4 and -4 μm. Bottom panel: Line-cut data of the photocurrent

distribution along the y-axis. (c-d) Photocurrent I_{ph} with V_{sd} = -0.4 V (c) and +0.4 V (d) as a function of a quarter wave plate angle θ. In Figs.(c) and (d), top, middle, and bottom panel correspond to the data measured for the transverse beam spot position at x = 4, 0, and -4 μm, respectively. The corresponding schematics are shown on the right side of the data. Solid curves are fits to the data using Eq. (1).

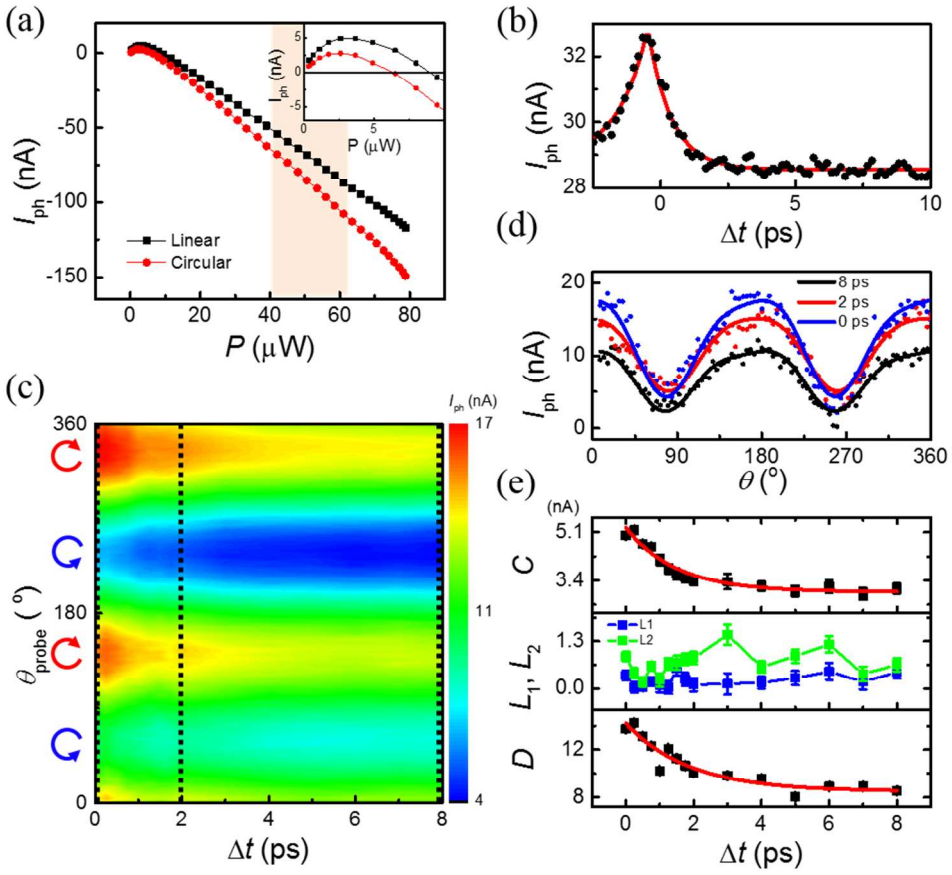

Figure 2. (a) Laser power P dependent I_{ph} at x = 0 μm with linearly (black) and circularly (red) polarized light when V_{sd} = 0 V. Shaded area denotes the specific range of power used in the experiment. Inset: A zoon-in view for P < 10 μW. (b) Time-resolved photocurrent trace is shown when temperature T = 77 K and V_{sd} = 0.4 V. The pump is linearly polarized (30 μW) and the probe is circularly polarized (30 μW). The Solid curve is an exponential fit with a best fitting

parameter of the relaxation time of 1.83 ps. (c) I_{ph} as a function of θ and Δt. The measurement conditions are: T = 77 K, V_{sd} = 0.3 V. (d) Line-cut of (c) at Δt = 0, 2, and 8 ps. (e) Time-dependent photocurrent component C, L_1, L_2, and D extracted from Eq. (1) is shown as a function of Δt. Note that we observe a similar relaxation time for C and D.

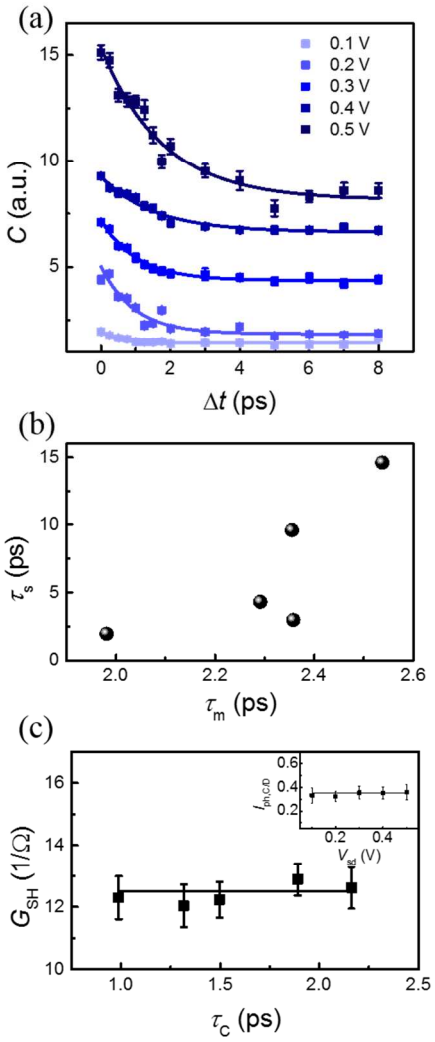

Figure 3. (a) Helicity-dependent photocurrent component C as a function of Δt in the range of V_{sd} from 0 to 0.5 V (from bottom to top curves). (b) The spin relaxation time τ_s was calculated using Eq. (2), and the data are plotted as a function of the momentum relaxation time τ_m. (c) Spin

Hall conductance G_{SH} is shown as a function of the helicity-dependent relaxation time τ_C. Inset: Charge-to-spin conversion efficiency $I_{ph,C/D}$ vs. V_{sd}.

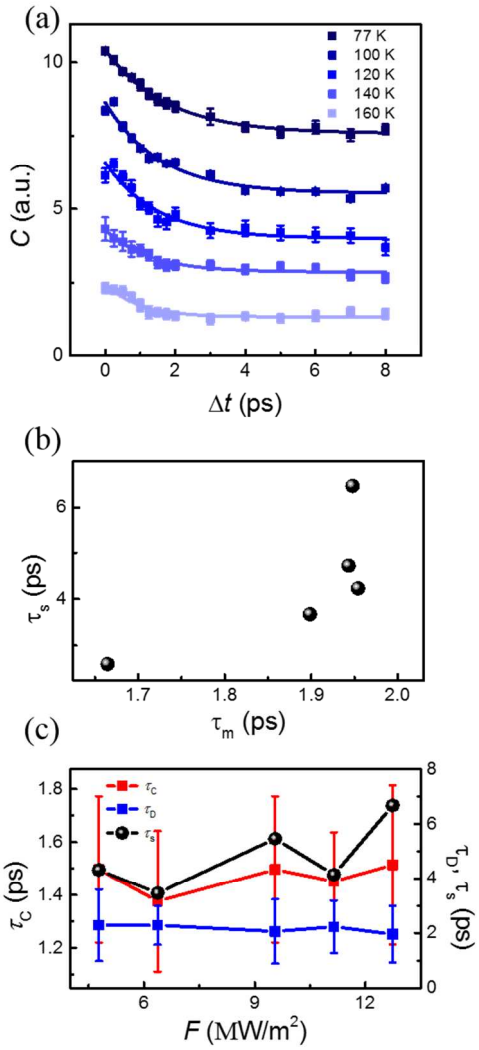

Figure 4. (a) Helicity-dependent photocurrent component C is shown as a function of Δt for several lattice temperature T. (b) Calculated τ_s using Eq. (2) is shown with respect to τ_m. (c)

Helicity dependent τ_C, helicity-independent τ_D, and τ_s are plotted as a function of the pump fluence F.

TABLE OF CONTENTS

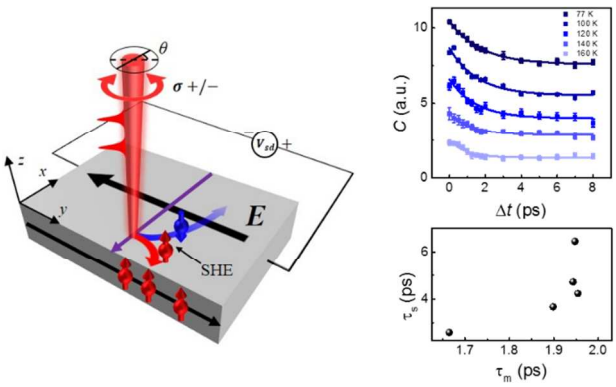

ASSOCIATED CONTENT

Supporting Information. Additional information provided. This material is available free of charge via the Internet at http://pubs.acs.org.

AUTHOR INFORMATION

Corresponding Author

*Email: hychoi@yonsei.ac.kr, dohunkim@snu.ac.kr

Notes

The authors declare no competing financial interest.

ACKNOWLEDGMENTS

J.L., S.S., S.P., S.C., S.L, C.I., S.C., and H.C. was supported by the National Research Foundation of Korea (NRF) through the government of Korea (MSIP) (grant nos. NRF-2016R1A4A1012929 and NRF-2015R1A2A1A10052520) and the Global Frontier Program (grant no. 2014M3A6B3063709). H.K. and J.S.K. were supported by SRC Center for Topological Matter (grant no. 2011-0030785) and Max-Plank POSTECH/KOREA Research Initiative (grant no. 2016K1A4A4A01922028). J.K. and D.L. were supported by the Basic Science Research Program through the NRF funded by MSIP (grant no. NRF-2015R1C1A1A02037430).

REFERENCES

(1) Huang, Y. Q.; Song, Y. X.; Wang S. M.; Buyanoa, I. A.; Chen. W. M. Spin injection and helicity control of surface spin photocurrent in a three dimensional topological insulator. *Nat. Commun.* **2017**, 8, 15401.

(2) Li, C. H.; van't Erve, O. M. J; Robinson, J. T.; Liu, Y.; Li, L.; Jonker, B. T. Electrical detection of charge-current-induced spin polarization due to spin-momentum locking in Bi_2Se_3. *Nat. Nanotechnol.* **2014**, 9(3), 218.

(3) McIver, J. W.; Hsieh, D.; Steinberg, H.; Jarillo-Herrero, P.; Gedik, N. Control over topological insulator photocurrents with light polarization. *Nature Nanotechnol.* 2012, 7(2), 96.

(4) Mellnik, A. R.; Lee, J. S.; Richardella, A.; Grab, J. L.; Mintun, P. J.; Fischer, M. H.; Vaezi, A.; Manchon, A.; Kim, E. –A.; Samarth, N. Spin-transfer torque generated by a topological insulator. *Nature* **2014**, 511(7510), 449.

(5) Pan, Y.; Wang, Q. Z.; Yeats. A. L.; Pillsbury, T.; Flanagan, T. C.; Richardella A.; Zhang, H.; Awschalom, D. D.; Liu, C. –X.; Samarth, N. Helicity dependent photocurrent in electrically gated $(Bi_{1-x}Sb_x)_2Te_3$ thin films. *Nat. Commun.* **2017**, 8(1), 1037.

(6) Tian, J.; Miotkowski, I; Hong, S.; Chen. Y. P. Electrical injection and detection of spin-polarized currents in topological insulator Bi_2Te_2Se. *Sci. Rep.* **2015**, 5, 14293.

(7) Kim, D.; Cho, S.; Butch, N. P.; Syers, P.; Kirshenbaum, K.; Adam, S.; Paglione, J.; Fuhrer, M. S. Surface conduction of topological Dirac electrons in bulk insulating Bi_2Se_3. *Nat. Phys.* **2012**, 8(6), 459.

(8) Hsieh, D.; Xia, Y.; Qian, D.; Wray, L.; Dil, J. H.; Meier, F.; Osterwalder, J.; Patthey, L.; Checkelsky, J. G.; Ong, N. P. A tunable topological insulator in the spin helical Dirac transport regime. *Nature* **2009**, 460(7259), 1101.

(9) Zhang, H.; Liu, C. –X.; Qi, X. –L.; Dai, X.; Fang, Z.; Zhang, S. –C. Topological insulators in Bi_2Se_3, Bi_2Te_3 and Sb_2Te_3 with a single Dirac cone on the surface. *Nat. Phys.* **2009**, 5(6), 438.

(10) Hasan, M. Z.; Kane, C. L. Colloquium: topological insulators. *Rev. Mod. Phys.* **2010**, 82(4), 3045.

(11) Pesin, D.; MacDonald, A. H. Spintronics and pseudospintronics in graphene and topological insulators. *Nat. Mater.* **2012**, 11(5), 409.

(12) Jamali, M.; Lee, J. S.; Jeong, J. S.; Mahfouzi, F.; Lv, Y.; Zhao, Z.; Nikolić, B. K.; Mkhoyan, K. A.; Samarth, N.; Wang, J. –P. Giant spin pumping and inverse spin Hall effect in the presence of surface and bulk spin-orbit coupling of topological insulator Bi_2Se_3. *Nano Lett.* **2015**, 15(10), 7126-7132.

(13) Kato, Y. K.; Myers, R. C.; Gossard, A. C.; Awschalom, D. D. Observation of the spin Hall effect in semiconductors. *Science* **2004**, 306(5703), 1910-1913.

(14) Sih, V.; Lau, W. H.; Mayers, R. C.; Gossard, A. C.; Awschalom D. D. Generating spin currents in semiconductors with the spin Hall effect. *Phys. Rev. Lett.* **2006**, 97(9), 096605.

(15) Sinova, J.; Valenzuela, S. O.; Wunderlich, J.; Back, C. H.; Jungwirth, T. Spin Hall effects. *Rev. Mod. Phys.* **2015**, 87(4), 1213.

(16) Stern, N. P.; Ghosh, S.; Xiang, G.; Zhu, M.; Samarth, N.; Awschalom, D. D. Current-induced polarization and the spin Hall effect at room temperature. *Phys. Rev. Lett.* **2006**, 97(12), 126603.

(17) Peng, X.; Yang, Y.; Singh, R. R. P.; Savrasov, S. V.; Yu, D. Spin generation via bulk spin current in three-dimentional topological insulators. *Nat. Commun.* **2016**, 7, 10878.

(18) Seifert, P.; Vaklinova, K.; Ganichev, S.; Kern, K.; Burghard, M.; Holleitner, A. W. Spin Hall photoconductance in a three-dimensional topological insulator at room temperature. *Nat. Commun.* **2018**, 9(1), 331.

(19) Noh, H. –J.; Jeong, J.; Cho, E. –J.; Park, J.; Kim, J. S.; Kim, I.; Park, B. –G.; Kim, H. –D. Controlling the evolution of tow-dimensional electron gas states at a metal/Bi_2Se_3 interface. *Phys. Rev. B.* **2015**, 91(12), 121110.

(20) Seifert, P.; Vaklinova, K.; Kern, K.; Burghard, M.; Holleitner, A. Surface state-dominated photoconduction and THz generation in topological Bi_2Te_2Se nanowires. *Nano Lett.* **2017**, 17(2), 973-979.

(21) Sim, S.; Koirala, N.; Brahlek, M.; Sung, J. H.; Park, J.; Cha, S.; Jo, M. –H.; Oh, S.; Choi, H. Tunable Fano quantum-interference dynamics using a topological phase transition in $(Bi_{1-x}In_x)_2Se_3$. *Phys. Rev. B.* **2015**, 91(23), 235438.

(22) Han, W.; Kawakami, R. K. Spin relaxation in single-layer and bilayer graphene. *Phys. Rev. Lett.* **2011**, 107(4), 047207.

(23) Boross, P.; Dóra, B.; Kiss, A.; Simon, F. A unified theory of spin-relaxation due to spin-orbit coupling in metals and semiconductors. *Sci. Rep.* **2013**, 3, 3233.

(24) Seki, T.; Hasegawa, Y.; Mitani, S.; Takahashi, S.; Imamura, H.; Maekawa, S.; Nitta, J.; Takanashi, K. Giant spin Hall effect in perpendicularly spin-polarized FePt/Au devices. *Nat. Mater.* **2008**, 7(2), 125.

(25) Pai, C. –F.; Liu, L.; Li, Y.; Tseng, H. W.; Ralph, D. C.; Buhrman, R. A. Spin transfer torque devices utilizing the giant spin Hall effect of tungsten. *Appl. Phys. Lett.* **2012**, 101(12), 122404.

(26) Lesne, E.; Fu, Y.; Oyarzun, S.; Rojas-Sánchez, J. C.; Vaz, D. C.; Naganuma, H.; Sicoli, G.; Attané, J. –P.; Jamet, M.; Jacquet, E. Highly efficient and tunable spin-to-charge conversion through Rashba coupling at oxide interfaces. *Nat. Mater.* **2016**, 15(12), 1261.

(27) Kim, D.; Li, Q.; Syers, P.; Butch, N. P.; Paglione, J.; Sarma, S. D.; Fuhrer, M. S. Intrinsic electron-phonon resistivity of Bi_2Se_3 in the topological regime. *Phys. Rev. Lett.* **2012**, 109(16), 166801.